

Influences from solvents on charge storage in titanium carbide MXenes

Xuehang Wang¹, Tyler S. Mathis¹, Ke Li¹, Zifeng Lin^{2,3}, Lukas Vlcek^{4,5}, Takeshi Torita⁶, Naresh C. Osti⁷, Christine Hatter¹, Patrick Urbankowski¹, Asia Sarycheva¹, Madhusudan Tyagi^{8,9}, Eugene Mamontov⁷, Patrice Simon^{2,10} and Yury Gogotsi^{1*}

Pseudocapacitive energy storage in supercapacitor electrodes differs significantly from the electrical double-layer mechanism of porous carbon materials, which requires a change from conventional thinking when choosing appropriate electrolytes. Here we show how simply changing the solvent of an electrolyte system can drastically influence the pseudocapacitive charge storage of the two-dimensional titanium carbide, Ti_3C_2 (a representative member of the MXene family). Measurements of the charge stored by Ti_3C_2 in lithium-containing electrolytes with nitrile-, carbonate- and sulfoxide-based solvents show that the use of a carbonate solvent doubles the charge stored by Ti_3C_2 when compared with the other solvent systems. We find that the chemical nature of the electrolyte solvent has a profound effect on the arrangement of molecules/ions in Ti_3C_2 , which correlates directly to the total charge being stored. Having nearly completely desolvated lithium ions in Ti_3C_2 for the carbonate-based electrolyte leads to high volumetric capacitance at high charge-discharge rates, demonstrating the importance of considering all aspects of an electrochemical system during development.

Growing demand for fast-charging electrochemical energy storage devices with long cycle lifetimes for portable electronics has led to a desire for alternatives to current battery systems, which store energy via slow, diffusion-limited Faradaic reactions. The devices that fit these demands most closely are electrochemical double-layer capacitors (EDLCs), also called supercapacitors, which can be fully charged within minutes with almost unlimited cyclability. However, the energy that can be stored via physisorption of ions at the pore walls of the porous carbons currently used in supercapacitor electrodes is much lower than the charge stored in battery materials, making them unsuitable replacements for many applications¹. Replacing the carbon electrodes in supercapacitors with pseudocapacitive materials results in devices with the potential for higher energy storage capabilities versus devices using EDLC-type materials². Unlike the diffusion-controlled intercalation of charge-storing ions into the crystal structure of battery materials, pseudocapacitive charge storage is defined by fast surface-confined redox reactions, which enable high-rate energy storage. The most prevalent mindset for designing energy storage systems is that the choice of electrode material is the dominant factor in determining the mechanism by which charge will be stored^{3,4}. Bulky materials, such as graphite, tin and silicon, are battery anode materials with diffusion-controlled intercalation⁵, where the insertion of ions into the bulk of these types of material leads to phase transformations and requires a large overpotential as the driving force to overcome the intercalation energy barrier in the material lattice. Surface-functionalized two-dimensional (2D) materials, e.g. reduced graphene oxide⁶, allow for the insertion of ions between their layers

with relative ease, but mainly double-layer capacitive charge storage has been observed for these materials unless the electrode surface is modified by pseudocapacitive materials (metal oxide or sulfide nanoparticles, redox-active conducting polymers or organic molecules) or if a redox-active electrolyte is used^{7,8}. Materials with intrinsic pseudocapacitive behaviour, such as RuO_2 , MnO_2 , Nb_2O_5 , conductive polymers and VN ^{9–11}, usually feature the presence of fast intercalation tunnels or surface redox reactions. However, most of these materials, with the exceptions of costly RuO_2 and VN , have limited electronic conductivity, limiting the high-power capabilities of devices made using these materials.

MXenes, a class of 2D materials with values of electrical conductivity up to $10,000\text{ S cm}^{-1}$, have shown potential as pseudocapacitive electrode materials in acidic aqueous electrolytes¹², where the MXene Ti_3C_2 has demonstrated high volumetric capacitance, up to $1,500\text{ F cm}^{-3}$ (ref. 13). However, the small voltage window of aqueous electrolytes limited the maximum energy storage capability of these studies, leaving organic electrolytes as a better alternative for higher-energy applications. Before this study, limited intercalation, or no intercalation, was reported for Ti_3C_2 with organic electrolyte systems using organic cations where moderate capacitance values were reported ($70\text{--}85\text{ F g}^{-1}$ at 2 mV s^{-1})^{14,15}. Another study reported higher capacitance values (200 F g^{-1} , or 80 F cm^{-3} , at 0.2 mV s^{-1}) for half-cells with electrodes made from multilayer Ti_3C_2 and using a typical battery electrolyte, lithium hexafluorophosphate in ethylene carbonate/dimethyl carbonate¹⁶. Their further demonstration of a hybrid Li-ion capacitor using a Ti_3C_2 negative electrode and a battery-type material for the positive electrode shows the potential

¹A. J. Drexel Nanomaterials Institute and Department of Materials Science and Engineering, Drexel University, Philadelphia, PA, USA. ²Materials Science Department—CIRIMAT, Université Paul Sabatier, Toulouse, France. ³Department of Materials Science and Engineering, Sichuan University, Chengdu, China. ⁴Materials Science and Technology Division, Materials Theory Group, Oak Ridge National Laboratory, Oak Ridge, TN, USA. ⁵Joint Institute for Computational Sciences, University of Tennessee, Knoxville, Oak Ridge, TN, USA. ⁶Murata Manufacturing Co., Ltd, Nagaokakyo-shi, Kyoto, Japan. ⁷Neutron Scattering Division, Oak Ridge National Laboratory, Oak Ridge, TN, USA. ⁸NIST Center for Neutron Research, National Institute of Standards and Technology, Gaithersburg, MD, USA. ⁹Department of Materials Science and Engineering, University of Maryland, College Park, MD, USA. ¹⁰Réseau sur le Stockage Electrochimique de l'Energie (RS2E), CNRS FR3459, Amiens, France. *e-mail: gogotsi@drexel.edu

that MXenes can have in these applications. These previous reports examined to some extent the mechanisms by which charge was stored in the MXenes that were used, and they showed variations in the interlayer spacing of the MXene during cycling, mentioning that the intercalation of charge-storing ions was accompanied by the penetration of solvent molecules into the MXene interlayer spaces. However, these reports did not consider the effects that making changes to their electrolyte chemistry could have had upon the electrochemical responses of their systems.

In this study, we demonstrate that the choice of the electrolyte solvent plays a significant role in determining the Li-ion intercalation process for Ti_3C_2 MXene electrode in organic electrolytes. During cycling using an electrolyte of lithium bis(trifluoromethylsulfonyl) amine (LiTFSI) in propylene carbonate (PC), the Li ions present in the interlayer space of the Ti_3C_2 are found to be fully desolvated, leading to a charge-storage mechanism dominated by pseudocapacitive intercalation. Replacing the PC solvent with acetonitrile (ACN) or dimethyl sulfoxide (DMSO) leads to a drastic capacitance decrease due to Li ions pulling solvent molecules into the interlayer spaces of Ti_3C_2 . This result is contrary to expectations based on carbon supercapacitor research, where ACN, with the highest ionic conductivity, should be the best solvent choice for a supercapacitor electrolyte⁷. We show that properly matching the electrolyte composition to the electrode material is essential for controlling the charge-storage mechanism and is necessary for achieving superior electrochemical performance.

Distinct charging processes for different solvent systems

To facilitate infiltration of the organic electrolytes into the layered Ti_3C_2 , a macroporous Ti_3C_2 (Supplementary Fig. 1) was used as the working electrode material. Figure 1a shows a comparison of cyclic voltammograms (CVs) at 2 mV s^{-1} for macroporous Ti_3C_2 electrodes tested in three 1M LiTFSI organic electrolytes with different solvents, DMSO, ACN and PC. Electrodes cycled in the PC-based electrolyte showed higher Coulombic efficiency (96%), and a wider negative voltage window of 2.4V when compared with the electrodes cycled in DMSO (2.1V) and ACN (2.2V). Chronoamperometry tests confirm a smaller steady-state leakage current value in the PC system ($-12.5\ \mu\text{A cm}^{-2}$) at -2.4 V versus Ag when compared with the other two electrolytes (Fig. 1b). All three systems showed leakage current densities smaller than $-30\ \mu\text{A cm}^{-2}$, indicating negligible contributions from any side reactions at their applied maximum voltage.

The discharge capacitance (charge delivered) at 2 mV s^{-1} , calculated by integrating the anodic scans of the CVs in Fig. 1a, is 130 F g^{-1} (273 C g^{-1}), 110 F g^{-1} (242 C g^{-1}) and 195 F g^{-1} (468 C g^{-1}) in LiTFSI–DMSO, LiTFSI–ACN and LiTFSI–PC, respectively. As the applied potentials are negative relative to the open-circuit voltage (OCV), lithium ion intercalation dominates the charging process. In general, ions with smaller size are beneficial for the electrical double-layer capacitance¹⁷. Partial or complete removal of the solvation shell of ions inserted into micropores may also enhance capacitance¹⁸. However, the choice of the solvent, which is not directly involved in charge storage, seems less important for the charge-storage capability of the electrode. The solvents' ionic conductivity is considered to profoundly affect the rate capability of the electrode, but no more consideration is given beyond that⁷. When compared with a PC-based electrolyte, ACN-based and DMSO-based LiTFSI electrolytes have higher ionic conductivity¹⁹, which correlates to better ion transport ability in the bulk electrolyte. Surprisingly, on the same macroporous Ti_3C_2 , the PC-based electrolyte stores 71% and 93% more charge than the DMSO- and ACN-based electrolytes, respectively, demonstrating that the solvent of the electrolyte is capable of strongly influencing the electrochemical performance.

The shapes of the CVs, which reflect the charging mechanism^{4,20}, also show a strong dependence on the electrolyte composition used

with the Ti_3C_2 negative electrode. In the LiTFSI–DMSO electrolyte, the CV in Fig. 1a shows characteristics of capacitive-dominant behaviour in the potential range of OCV to -1.2 V versus Ag, with slowly increasing intercalative behaviour. Then, the charging process evolves into an intercalation-like mechanism below -1.2 V versus Ag, with visible redox peaks being seen. Galvanostatic charge–discharge (GCD) tests for the DMSO-based electrolyte also confirm two stages of charging (Supplementary Fig. 2). When LiTFSI–ACN was used as electrolyte, the CV showed the same initial features, that is capacitive-dominant behaviour at more positive potentials and a stronger intercalation feature at higher states of charging. However, when compared with the DMSO-based electrolyte, the electrochemical signature of the ACN system at higher states of charge (negative potentials) suggests sluggish electrochemical reaction kinetics, as can be seen from the lower current and the presence of broad peaks; this is also visible in the GCD tests, which show a nearly linear dependence of the potential on time.

In comparison, voltammograms of Ti_3C_2 in LiTFSI/PC electrolyte show different features, with two pairs of symmetric peaks during cycling, indicating that the charging process is dominated by fast redox reactions associated with the intercalation processes. The contribution of electrical double-layer capacitance to the overall capacitance is discussed in Supplementary Discussion 1. The cathodic intercalation process starts at about -0.3 V and expands gradually down to -1.5 V versus Ag. Below -1.5 V versus Ag, the process is similar to what was observed in the DMSO-based electrolyte. However, the higher current shows that there is improved electrochemical activity for the PC system. Interestingly, the redox peaks at about -1.5 V versus Ag are shifted to higher potential in the PC system when compared with DMSO. Also, the peak potential difference between the anodic and cathodic peaks (ΔE_p) is lower than that of DMSO: $\Delta E_p = 0.35\text{ V}$ and 0.5 V in PC- and DMSO-based electrolytes, respectively. This suggests faster electrochemical reaction kinetics in the PC-based electrolyte.

Electrochemical impedance spectroscopy (EIS) measurements were performed for each of the three electrolytes at OCV and the maximum negative potential. The equivalent series resistance, taken from the real-axis intercept of the Nyquist plots in Fig. 1c, increases for the solvents used in this study in the following order: ACN, DMSO and then PC, in agreement with the trend of decreasing electrolyte conductivity¹⁹. At OCV, the Ti_3C_2 electrode shows typical capacitive behaviour in both DMSO- and PC-based electrolytes, with a small loop in the high-frequency region associated with interfacial impedance at the electrode/current-collector interface, followed by a sharp increase at low frequencies. The inset of Fig. 1c shows that there is a small region with a 45° slope in the mid-frequency range, indicating that there are similar ion diffusion limitations for the PC and DMSO systems at their resting potentials. In contrast, the EIS plot of the ACN system shows a deviation from ideal capacitive behaviour in the low-frequency region, with a nearly constant increase of both the imaginary and the real parts of the impedance^{21,22}. This is evidence that the solvent in the ACN system limits the accessibility and transport of lithium ions inside the porous structure of the Ti_3C_2 electrode, contrary to what would be expected on the basis of the high ionic conductivity of ACN-based electrolytes. When the EIS spectra were recorded at the maximum negative potential of each system (Fig. 1d), all the Nyquist plots showed deviations from capacitive behaviour in the low-frequency region and slightly higher ion diffusion resistance (45° linear part) when compared with the spectra taken at OCV. These observations are consistent with the idea that the charge-storage mechanism of the Ti_3C_2 electrode is not a purely capacitive process.

Molecular arrangements of electrolytes in MXenes

To facilitate a more fundamental understanding of the distinct charging processes for the different solvent systems, in situ X-ray

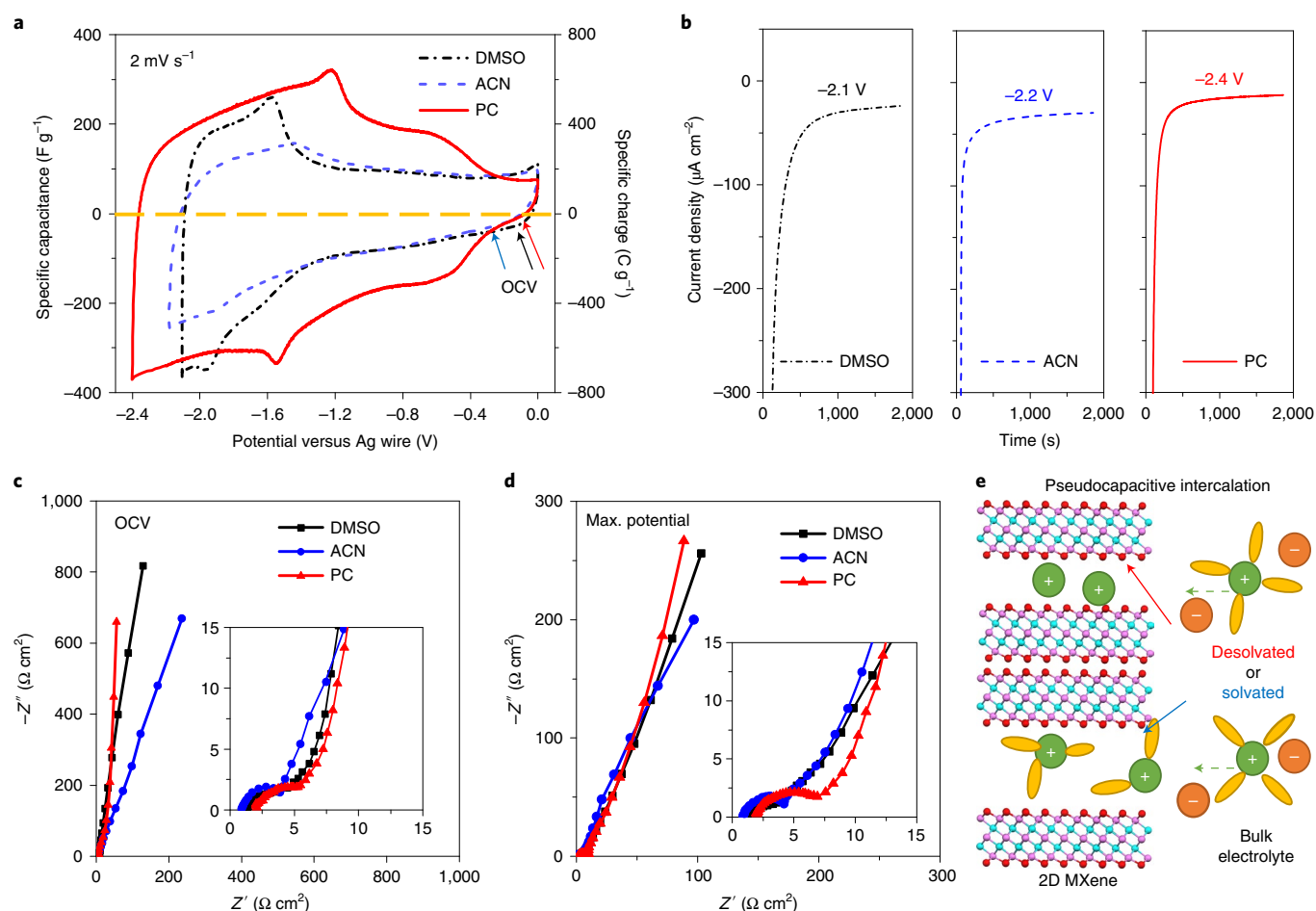


Fig. 1 | Macroporous Ti_3C_2 electrode with 1M LiTFSI in DMSO, ACN and PC organic electrolytes. a, CV curves. The OCVs (marked by arrows) are -0.13 V (black), -0.32 V (blue) and -0.12 V (red) versus Ag for DMSO, ACN and PC-based electrolytes, respectively. **b,** Chronoamperometry data collected at the applied maximum potentials. **c,** EIS data collected at the OCV. **d,** EIS data collected at the maximum negative potential versus Ag. The insets in **c** and **d** show the magnified curves in the high-frequency range; they use the same units as in **c** and **d**. **e,** Schematic of a supercapacitor using 2D MXene (pink, Ti; cyan, C; red, O) as negative electrode with solvated or desolvated states. Legend for the electrolyte: green, cation; orange, anion; yellow, solvent molecule.

diffraction (XRD) measurements were made to track the evolution of the interlayer space of the Ti_3C_2 electrodes during cycling (as illustrated in Fig. 1e). The d -spacing for the DMSO system varied between 18.8 and 19.3 Å during cycling (Fig. 2a). During charging (cathodic polarization), the d -spacing increased from the minimum value of 18.8 Å to reach a maximum of 19.3 Å at -1 V , and then decreased to 19.0 Å for the fully charged state. The critical turning point from enlargement to shrinkage of interlayer space occurring at -1 V versus Ag may be correlated to the onset of a state where a substantial number of Li ions have been intercalated. These intercalated Li ions will attract the MXene layers to each other, resulting in a reduced interlayer space²³. Alternatively, some solvent molecules may be pushed out from the interlayer space with the increasing number of ions between the MXene sheets. Upon discharging, this process was exactly reversed, indicating that the cycling process is highly symmetric for the DMSO system. In ACN, the d -spacing changes between 13.0 and 13.4 Å, where the maximum d -spacing is noticeably smaller than even the minimum d -spacing of the DMSO system. Additionally, a small invariable peak at 8.2° can be observed in the ACN system during cycling, which indicates that a minor proportion of the electrode material has a constant interlayer spacing of 10.7 Å (Supplementary Fig. 3). A unique situation occurred for the PC system, where the d -spacing of the Ti_3C_2 stayed constant at 10.7 Å during cycling as shown in Fig. 2c, which is similar to the pristine Ti_3C_2 used in this

study (10.6 Å, Supplementary Fig. 4). Notably, ex situ characterization, including Raman spectroscopy (Supplementary Fig. 5), X-ray photoelectron spectroscopy (XPS, Supplementary Figs. 6 and 7) and transmission electron microscopy (TEM, Supplementary Fig. 8), verified that the differences in electrochemical signature and in interlayer spacing changes for the three systems were not related to irreversible chemical changes occurring in the Ti_3C_2 during cycling (For details see Supplementary Discussion 2).

When compared with the PC-based system with a larger stored charge but unchanged interlayer space, the expansion of the interlayer space in both DMSO- and ACN-based systems indicates the co-intercalation of solvent molecules into the MXene electrode together with Li ions. Molecular dynamics (MD) simulations were performed to better understand the role the solvents have in influencing the interlayer spacing and electrochemical responses of Ti_3C_2 during cycling. The simulation suggests that about 1.3 DMSO molecules per Li^+ are needed to reproduce the large interlayer spacing for the DMSO system (Fig. 2d). In the charged state, the electrolyte forms a structure in which the oxygen atoms of DMSO are oriented to interact with intercalated Li ions at the Ti_3C_2 electrode surface, which results in the hydrophobic CH_3 groups of the solvent molecules being directed away from the electrode surface. This creates a hydrophobic environment, illustrated in Fig. 2d, in between two layers of solvents within the interlayer space of the Ti_3C_2 .

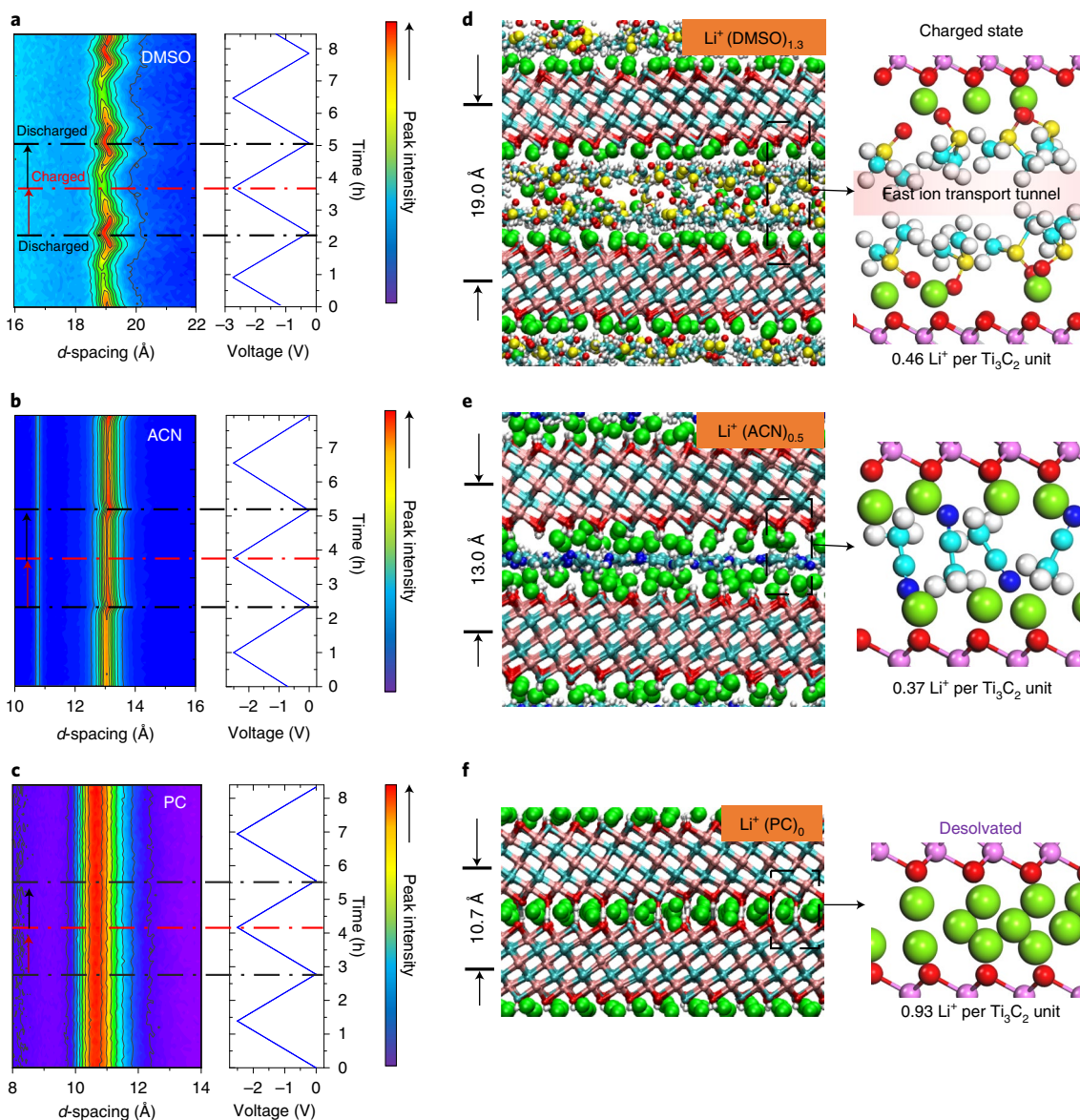


Fig. 2 | *d*-spacing evolution during cycling and molecular arrangements. **a**, In situ XRD map of vacuum-filtered Ti_3C_2 in DMSO-based electrolyte. **b**, In situ XRD map of vacuum-filtered Ti_3C_2 in ACN-based electrolyte. **c**, In situ XRD map of vacuum-filtered Ti_3C_2 in PC-based electrolyte. The right-hand curves in **a–c** show the cycling process during XRD analysis. **d**, MD simulation result for DMSO-based electrolyte, showing a MXene/ Li^+ /DMSO/fast ion transport tunnel/DMSO/ Li^+ /MXene structure. **e**, MD simulation result for ACN-based electrolyte, showing a MXene/ Li^+ /ACN/ Li^+ /MXene structure. **f**, MD simulation result for PC-based electrolyte, showing a MXene/ Li^+ /MXene structure. The magnified local molecular arrangements in **d–f** are shown as schematics to the right of their MD simulation results. Legend for **d–f**: green, Li^+ ; pink, Ti; cyan, C; red, O; teal, F; white, H; yellow, S; blue, N, with the size of the lithium atoms increased for clarity in the simulated images. The MD simulations in **d–f** were performed on the basis of the experimental values of the interlayer spacing and the charge stored in the macroporous Ti_3C_2 .

Temperature-dependent quasi-elastic neutron scattering (QENS) measurements made using a neutron backscattering spectrometer show that the methyl group dynamics remains almost unchanged in the charged and discharged DMSO-based system, when compared with the bulk solvent (Supplementary Fig. 9a). This finding suggests that the methyl groups of the intercalated DMSO molecules are as free during charge–discharge as those of the bulk electrolyte, which strongly supports the notion of a hydrophobic environment being formed by the methyl groups. In this environment, any Li^+ entering the electrode has weakened electrostatic interactions with both the distant charged electrode surface and the hydrophobic CH_3 groups, which makes this environment an efficient tunnel for transport of lithium ions. This model environment fits well with the capacitive behaviour of the DMSO system in Fig. 1a,c.

With the smaller *d*-spacing of the ACN electrolyte system, the calculated ratio of Li^+ to ACN molecules is only 1:0.5. This is a much lower solvation level when compared with the DMSO-based system and allows for only a single layer of ACN solvent in between Ti_3C_2 layers (Fig. 2e). The smaller rod-like ACN molecules with a single hydrophobic CH_3 group cannot easily form a continuous hydrophobic layer as in the case of DMSO, but rather tend to align parallel to the Ti_3C_2 surfaces. On the basis of QENS, the methyl dynamics of ACN almost completely vanished in the charged and discharged samples, which contrasts with the fairly strong signal seen in the bulk ACN at 80 K (Supplementary Fig. 9b). Compared with the highly mobile methyl group in the DMSO, the very low mobility of the methyl group in ACN agrees with the simulated structure without a continuous hydrophobic layer. Such a solvent arrangement

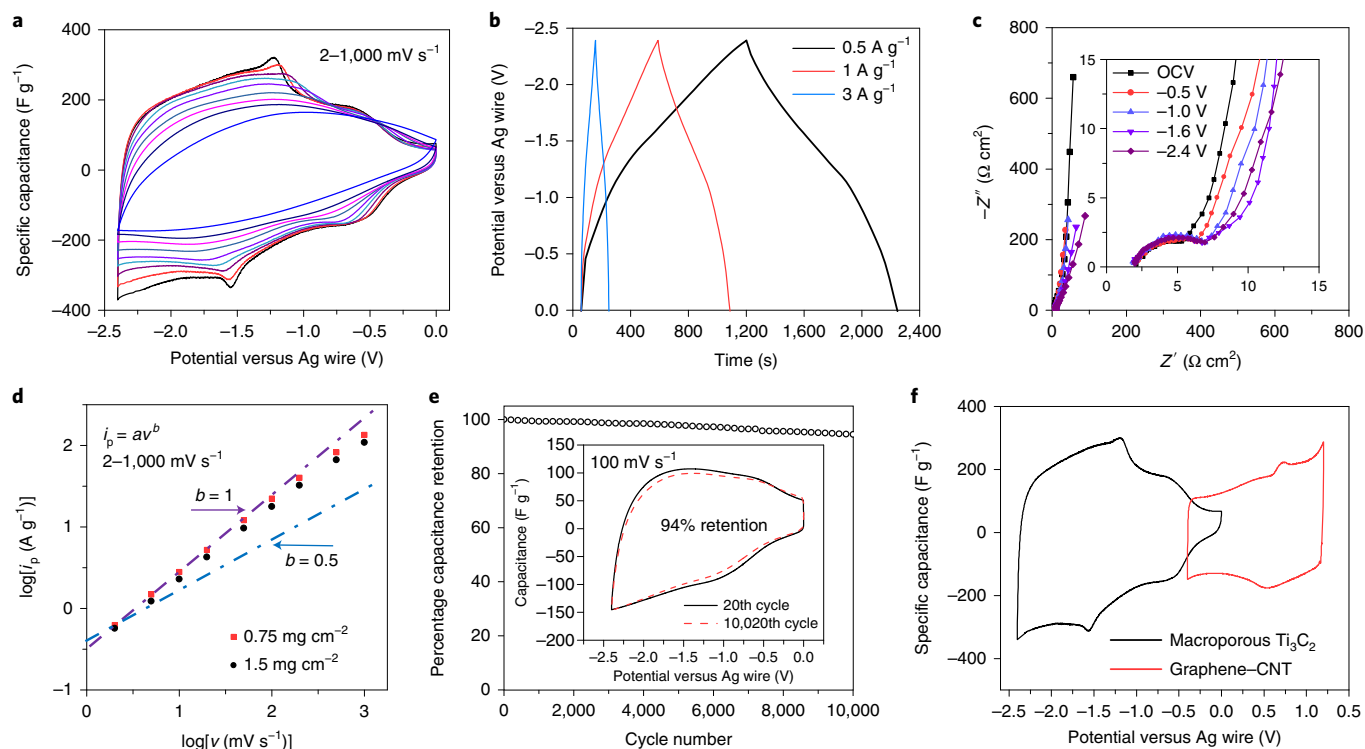


Fig. 3 | Electrochemical performance of the macroporous Ti_3C_2 in LiTFSI with PC solvent. **a**, Three-electrode CV curves: the scan rates from outer cycle to inner cycle are 2, 5, 10, 20, 50, 100, 200, 500 and 1,000 mV s^{-1} . **b**, Three-electrode galvanostatic charge-discharge curves with current densities of 0.5, 1 and 3 A g^{-1} . **c**, Impedance spectra collected at different potentials for the LiTFSI-PC electrolyte. The inset shows the magnified curve in the high-frequency range. **d**, Determination of the slope, b value, for the logarithm of anodic peak (discharge) current (i_p) versus logarithm of scan rate (ν) from 2 to 1,000 mV s^{-1} with mass loadings of 0.75 mg cm^{-2} and 1.5 mg cm^{-2} . $b = 1$ indicates non-diffusion-limited capacitive storage and $b = 0.5$ means diffusion-limited processes. **e**, Cycling stability at 100 mV s^{-1} for 10,000 cycles; the inset shows the CVs of the 20th cycle and the 10,020th cycle. **f**, Full cell fabrication: three-electrode CV of the macroporous Ti_3C_2 MXene (195 F g^{-1} , 410 F cm^{-3}) and graphene-CNT composite electrodes (144 F g^{-1} , 230 F cm^{-3}) at 2 mV s^{-1} .

within the Ti_3C_2 layers would severely hinder the mobility of lithium ions during Li^+ insertion/de-insertion, which agrees well with the distorted CVs at high polarization (Fig. 1a) and deviations from capacitive behaviour at low frequencies on the EIS curve (Fig. 1c).

The modelled situation for the PC electrolyte system (Fig. 2f) again differs significantly from both the ACN and DMSO systems. The in situ XRD results show that the d -spacing for this system remains constant at 10.7 \AA (an interlayer spacing of $<2.9 \text{ \AA}$) during cycling. This small interlayer spacing in the PC system cannot accommodate any solvent molecules with the intercalated lithium ions, meaning that the Li^+ in between the Ti_3C_2 layers should be fully desolvated. The mean squared displacement measured by QENS shows that the PC molecules are less tightly confined than the ACN molecules (Supplementary Fig. 9c and Supplementary Fig. 10), despite the smallest interlayer space for the PC electrolyte. This agrees with there being no PC molecules residing between the Ti_3C_2 layers. As discussed in Supplementary Discussion 3, neither solid-electrolyte interphase formation nor the solvent-ion interaction alone can explain the complete desolvation of Li ions from the PC electrolyte. The combination of these factors, as well as the solvent-MXene interactions, is probably the reason for the observed behaviour. However, further studies of interactions in various ion-MXene-solvent systems are certainly needed. With such solvent-free Li ions in the interlayer spaces, the charging process in Ti_3C_2 in PC-based electrolyte appears to be very similar to the Li^+ intercalation process in a bulk material of a battery anode²⁴. However, unlike a real battery, the Ti_3C_2 electrode still showed pseudocapacitive features in its impedance spectra (Fig. 1c), due to the 2D structure of the Ti_3C_2 materials, which offers highly accessible redox-active sites. Additionally, the pseudocapacitive feature with

low diffusion resistance could benefit from the high conductivity of the Ti_3C_2 electrode itself¹², and possibly a partial breaking of the Coulombic effect at high confinement²⁵.

The distinct electrolyte arrangements between the Ti_3C_2 layers for each solvent system not only influence the ionic transport, but also significantly influence the total amount of charge able to be stored by the electrode. The number of intercalated lithium atoms, calculated on the basis of the pseudocapacitive charge per gram of macroporous Ti_3C_2 , turns out to be 0.93 per Ti_3C_2 unit for the PC-based electrolyte, which is more than double that for the other electrolyte systems (0.46 and 0.37 for DMSO and ACN electrolytes, respectively). Unlike three-dimensional materials with fixed pore sizes, the expandability of the interlayer spacing of MXenes has been demonstrated during electrochemical cycling in both aqueous and ionic liquid electrolytes^{26–28}. Previously reported strategies for increasing the charge-storage capabilities of 2D materials have focused on increasing their interlayer spacing to increase the accessible surface area and improve ion transport rates. This thought process holds true when comparing the electrolyte structure in the DMSO system, with the largest interlayer spacing in this study, which offers lower ion transfer resistance and higher capacitance than the ACN system. However, the highest capacitance is achieved in the fully desolvated PC system, which contrasts starkly with the DMSO system. Li ions that have been completely stripped of their solvation shell can attach strongly to both pore surfaces at the same time, which should be favourable for additional Li^+ to enter the interlayer spaces of the Ti_3C_2 . This also helps explain why the intercalation-type electrochemical response starts at a potential very close to the resting potential in the PC-based electrolyte in Fig. 1a. For the other electrolyte systems, the presence of solvent molecules

sterically hinders the access of Li^+ , and Li^+ can only be attached to one of the interlayer surfaces, as the co-intercalated solvent molecules drive the Ti_3C_2 layers apart.

Full desolvation towards enhanced energy storage in MXene

A full electrochemical evaluation of a macroporous Ti_3C_2 electrode, including rate capability, cycling stability and full cell performance, was conducted using the PC-based electrolyte to demonstrate the full capabilities of this system. In Fig. 3a, the two sets of reversible redox peaks in the CVs are visible for the anodic and cathodic sweeps with a small peak potential separation when cycling at 2 mV s^{-1} , indicating that this is a fast, non-diffusion-limited pseudo-intercalation mechanism^{2,20,29}. The nonlinear GCD curve without a plateau (Fig. 3b) and the nearly vertical EIS curve in the low-frequency region for the charged states (Fig. 1c) further show that Ti_3C_2 stores charge pseudocapacitively. As the state of charge increases, the impedance spectra in the low-frequency region gradually deviate further from ideality, with the greatest shifts seen at -1.6 V and -2.4 V versus Ag. This fits well with the strong intercalation reactions that occur from -1.5 V versus Ag on the CV curve. The b value, which is used to distinguish between battery-like (diffusion-controlled) and supercapacitor-like behaviours¹⁴, was evaluated on the basis of the current density at the highest peak for Ti_3C_2 electrodes. The b value of Ti_3C_2 MXene is very close to 1 in a large range of scan rate from 2 to $1,000\text{ mV s}^{-1}$, as shown in Fig. 3d and Supplementary Fig. 11a; this is characteristic of a non-diffusion-limited pseudocapacitive intercalation process.

The capacitance of the electrode (mass loading = 0.75 mg cm^{-2}) at 2 mV s^{-1} was calculated to be 195 F g^{-1} (410 F cm^{-3}) over a voltage window of 2.4 V . When the scan rate increases to $1,000\text{ mV s}^{-1}$, the capacitance remains at 120 F g^{-1} (252 F cm^{-3}), a capacitance retention of 61% relative to the value at 2 mV s^{-1} , an impressive result considering this is a 2D material in an organic electrolyte. Doubling the electrode mass loading results in a capacitance retention of 58% at $1,000\text{ mV s}^{-1}$, showing a weak dependence of the capacitance retention on electrode thickness for the range of mass loadings used in this study (Supplementary Fig. 11b,c). The charge stored in the pseudocapacitive MXene electrode, or the capacity (mAh g^{-1}), was evaluated by using GCD curves (on the basis of Equation 2) at current densities from 0.5 A g^{-1} to 100 A g^{-1} (Supplementary Fig. 12). The capacity of the macroporous Ti_3C_2 electrode was 145 mAh g^{-1} at 0.5 A g^{-1} ($\approx 3.5\text{ C rate}$) and 100 mAh g^{-1} at 100 A g^{-1} ($\approx 700\text{ C}$), or a 71% capacity retention. Supplementary Fig. 11d shows the volumetric capacitance at different scan rates in comparison with literature reports on materials with high volumetric capacitance in organic electrolytes, demonstrating the improvements that the macroporous Ti_3C_2 electrode material in the PC-based electrolyte has made over previous studies. The cycling life of the electrode was tested with a voltage window of 2.4 V and a scan rate of 100 mV s^{-1} . The Ti_3C_2 electrode showed a good cycling stability of 94% capacitance retention after 10,000 cycles (Fig. 3e). The stability of the Ti_3C_2 electrode was also evaluated using floating tests (Supplementary Fig. 13), which resulted in 96% capacitance retention after 120 h of floating with a slightly smaller (-0.01 A g^{-1}) leakage current when compared with the first loop. An asymmetric full cell was made with Ti_3C_2 as the negative electrode and a graphene-carbon nanotube composite (graphene-CNT) as the positive electrode to further evaluate the Ti_3C_2 pseudocapacitive electrode in a practical manner (Fig. 3f). The advantageous energy density versus power density of the full cell (Supplementary Fig. 14) demonstrates how getting the right combination of electrode material and electrolyte can improve the electrochemical performance of the final device.

Conclusions

We have demonstrated that correctly coupling organic electrolytes with 2D Ti_3C_2 electrodes is dominant in determining the

electrochemical charge-storage mechanism. The choice of solvent has been proven to be capable of controlling ion transport and intercalation with distinct evolutions in the interlayer spacing. Remarkably, the PC- Ti_3C_2 system brings about efficient desolvation during charging, resulting in high volumetric charge-storage capability and fast charge transport. With minimized interlayer distance, maximized capacitance and good rate performance, this charging behaviour provides new insights for energy storage in 2D materials by efficiently coupling electrolytes and electrode materials. This study also demonstrates a rational design routine for coupling electrode materials with optimized electrolytes.

Methods

Preparation of Ti_3C_2 colloidal solution. Multilayer Ti_3C_2 was produced by etching Ti_3AlC_2 MAX phase in a mixture of HCl and LiF, similar to the method reported in our previous study³⁰. In detail, 1 g of LiF was added to 20 ml of 9M HCl solution, followed by a slow addition of 1 g of Ti_3AlC_2 with stirring in an ice bath. After etching at 35°C for 24 h, the multilayer Ti_3C_2 was washed with deionized water by centrifuging until the pH of the supernatant reached about 6. The sediment of the centrifuge (multilayer Ti_3C_2) was collected and dried in a desiccator under vacuum. The multilayer Ti_3C_2 was dispersed in deionized water before being bath sonicated for 1 h with Ar bubbling and ice bath. After centrifuging of the sonicated solution at $3,500\text{ rpm}$ for 1 h, the 'few-layer' Ti_3C_2 colloidal solution in water was collected as the dark supernatant.

Preparation of vacuum-filtered Ti_3C_2 thin film. 'Few-layer' Ti_3C_2 colloidal solution was vacuum filtered through a $25\text{ }\mu\text{m}$ thick Celgard 3501 polypropylene membrane. The wet Ti_3C_2 film on the Celgard was collected and dried in vacuum overnight at 80°C . The vacuum-filtered Ti_3C_2 thin film, with a density of 2.6 g cm^{-3} (Supplementary Fig. 1c), was collected by peeling the thin film off the Celgard.

Preparation of macroporous Ti_3C_2 . The polystyrene (PS) spheres were polymerized from styrene as reported by Park et al.³¹. In brief, 100 mg polyvinyl pyrrolidone and 102.6 mg ammonium persulfate were added to a 500 ml vial containing a solution of 230 ml ethanol and 30 ml deionized water. After stirring the mixture for 10 min at room temperature, 22 ml styrene monomer was added once with quick stirring at 70°C . The polymerization process continued for 24 h at 70°C in an oil bath, before it was ended by cooling the vial in an ice bath for 30 min. The PS spheres were collected by centrifuging and washing with deionized water and ethanol afterwards.

The 'few-layer' Ti_3C_2 colloidal solution was sonicated with PS spheres (the mass ratio between PS and Ti_3C_2 was 3:1) for 10 min. The colloidal mixture solution was vacuum filtered onto the Celgard and then vacuum dried in a desiccator overnight. A free-standing Ti_3C_2 -PS sphere film was peeled off from Celgard and annealed at 450°C for 1 h under an argon flow. After removing the PS by annealing, a free-standing templated porous Ti_3C_2 was prepared (Supplementary Fig. 1a). The macroporous Ti_3C_2 (Supplementary Fig. 1b) was obtained by further pressing the templated porous Ti_3C_2 film on a PET film under 3 MPa. The resulting film has a density of 2.1 g cm^{-3} , slightly lower than conventional vacuum-filtered Ti_3C_2 films ($2.6\text{--}3.0\text{ g cm}^{-3}$)³².

Preparation of graphene-CNT composites for positive electrode. Single-wall CNTs (1 mg, Tuball) were first dispersed in ethanol by probe sonication for 1 h. Then, 2 ml of 4.5 mg ml^{-1} graphene oxide aqueous solution (prepared according to ref. 33) was added to the mixture and probe sonicated for another 30 min. The mixture was further mixed with $70\text{ }\mu\text{l}$ ammonia solution (28 wt% in water) and $20\text{ }\mu\text{l}$ hydrazine solution (35 wt% in water) and heated at 95°C for 1 h without stirring to produce a homogeneous black graphene-CNT dispersion. A free-standing graphene-CNT film, with a density of 1.6 g cm^{-3} , was obtained by vacuum filtration and vacuum drying at 70°C for 24 h.

Material characterization. The morphology of Ti_3C_2 MXene was observed using scanning electron microscopy (Zeiss Surra 50VP). The MXene structure before and after cycling was confirmed via TEM (JEOL JEM-2100) operated at an accelerating voltage of 200 kV. The Ti_3C_2 MXene electrode was mounted in epoxy and allowed to cure for 24 h. TEM grids were prepared from epoxy-mounted samples using ultramicrotomy with a glass knife. Chemical compositions of the samples were further analysed by high-resolution XPS recorded with a Physical Electronics VersaProbe 5000 instrument equipped with a monochromatic Al K α X-ray beam ($h\nu = 1,486.6\text{ eV}$). Peak fitting was carried out using CasaXPS Version 2.3.16 RP 1.6. Raman spectra were recorded with a Renishaw Raman InVia confocal microscope. Laser excitation was 488 nm , grating 1200 gr mm^{-1} , 5% of laser power. A $\times 50$ lens was used.

For ex situ neutron scattering experiments, multilayered Ti_3C_2 MXene was rolled on to stainless steel mesh in a rolling machine and dried before being used as the supercapacitor electrode. The electrodes were cycled in a three-electrode cell

with activated carbon as the counter-electrode and LiTFSI–DMSO, LiTFSI–ACN and LiTFSI–PC as the electrolytes. For each electrolyte, one discharged electrode and one charged electrode (at its maximum voltage as shown in Fig. 1a) were directly disassembled from the cell, kept inside a Teflon-coated cylindrical aluminium sample holder to prevent a loss of charge during the measurement and sealed in helium atmosphere with indium inside a glovebox. Measurements of the temperature dependence of elastically scattered neutron intensity (all samples and an empty cell) were carried out using the high-flux backscattering spectrometer (HFBS) at the National Institute of Standards and Technology (NIST) Center for Neutron Research³⁴ by operating the instrument in fixed window mode. The temperature scan was performed with heating from 20 to 320 K at a rate of 1 K min⁻¹ under vacuum. The temperature was controlled using a closed-cycle helium refrigerator. The intensities of all detectors (16 detectors in total) were combined to obtain the final elastic intensity for a sample.

In situ XRD was carried out on a Bruker D8 diffractometer using a two-electrode Swagelok-derived electrochemical cell with Ti₃C₂ films as working electrodes and YP-50 carbon films as overcapacitive counter-electrodes. Vacuum-filtered Ti₃C₂ film electrodes with consistent flake alignment (Supplementary Fig. 1c) were used for in situ XRD measurements. The flake size (100–200 nm) and the *d*-spacing (~10.6 Å) of the vacuum-filtered Ti₃C₂ (Supplementary Fig. 4a) were the same as those of the macroporous Ti₃C₂ (Supplementary Fig. 4b) used in the section ‘Distinct charging processes for different solvent systems’. The CVs and Nyquist plots for the vacuum-filtered Ti₃C₂ electrodes in the different electrolytes are comparable to the results shown for macroporous Ti₃C₂ and are discussed in detail in the supplementary information (Supplementary Fig. 15). A beryllium window (allowing X-rays to easily penetrate) was used as the current collector for MXene electrodes. XRD (Cu Kα, λ = 0.154 nm) patterns were collected during cyclic voltammetry measurements with a slow scan rate of 0.5 mV s⁻¹ to ensure that enough patterns were recorded as well as small potential evolution (≈0.2 V) for each pattern. For MXene electrodes in 1 M LiTFSI in PC and ACN solvents, only the (002) peak located between 6° and 10° was selected for XRD analysis, while in 1 M LiTFSI in DMSO the (004) peak located around 9.8° was selected for XRD study due to the difficulty of collecting the (002) peak around 5°. The XRD patterns of three full cycles were recorded for each electrolyte to demonstrate that the changes in the electrodes’ interlayer spacing are consistent from cycle to cycle.

Electrode preparation. The working electrode was prepared by pressing the vacuum-filtered Ti₃C₂ thin film or the macroporous Ti₃C₂ onto a 316L stainless-steel mesh (100 mesh screen) under 8 MPa. The mass loading of the vacuum-filtered Ti₃C₂ thin film is 0.9 g cm⁻², and the macroporous Ti₃C₂ has a mass loading of either 0.75 or 1.5 g cm⁻². The counter-electrode is YP-50 activated carbon with 5% polytetrafluoroethylene (Sigma-Aldrich) binder added. The YP-50 activated carbon was rolled into a free-standing film and cut into disc-shaped electrodes before being pressed onto a carbon-coated aluminium foil current collector. A free-standing graphene–CNT film with a mass loading of 2.25 mg cm⁻² was also pressed onto the carbon-coated aluminium foil current collector and used as the positive electrode for a full cell. All electrodes were dried under vacuum for at least 12 h at 80 °C before use.

All cells were fabricated in a glovebox with controlled atmosphere of O₂ < 0.1 ppm and H₂O < 0.1 ppm (Vacuum Technologies). For a three-electrode cell, one working electrode and one overcapacitive counter-electrode were separated by two layers of Celgard, with a silver wire reference electrode in between the two layers of separators. For a two-electrode cell, one MXene electrode and one graphene–CNT electrode were separated by one layer of Celgard. After the electrolyte was added, the cell was clamped and packaged in a polyethylene terephthalate bag. Following assembly, all cells were stabilized overnight before the electrochemical tests.

Electrochemical tests. All electrochemical tests were performed on a Bio-Logic VMP3 potentiostat. Before the electrochemical tests, all electrodes were precycled 20 times to stabilize the performance (Supplementary Fig. 2b–d). Chronoamperometry tests were performed by applying a constant voltage to the three-electrode cell. The current responding to different constant voltages was recorded for 30 min. The CVs were tested with scan rates from 2 mV s⁻¹ to 1,000 mV s⁻¹, and a GCD test was performed at current densities from 0.5 to 100 A g⁻¹. The impedance spectroscopy was tested in a range of 10 mHz to 200 kHz under potential amplitude from OCV to the maximum applied voltage. Cycling stability was tested with a scan rate of 100 mV s⁻¹, and 60 s resting time was set between each cycles. The floating test, with five GCD cycles at 1 A g⁻¹ followed by 2 h maximum potential holding, was repeated for 60 loops, recording the capacitance during GCD cycling and the current responding (or current leakage) in the floating period of each loop.

Calculations for the electrochemical tests. The capacitance of a single electrode (*C_{sp}*) was calculated from the anodic scan of the CV curve on the basis of

$$C_{\text{sp}}(\text{F g}^{-1}) = \frac{\int i \, dt}{mV} \quad (1)$$

Here, *i* is the current changed by time *t*; *m* is the mass of a single electrode and *V* is the voltage window of the CV scan. The volumetric capacitance of a single electrode is calculated on the basis of *C_v* = *C_{sp}* × material density.

As the GCD curve is nonlinear, the capacity (mAh g⁻¹) of a single electrode, instead of the capacitance, is evaluated using

$$C (\text{mAh g}^{-1}) = \frac{I \, \Delta t}{3.6m} \quad (2)$$

where *I* is the constant current applied to the cell and Δ*t* is the discharging time.

For the two-electrode cell, the capacitance of the full cell was evaluated on the basis of the CV curve:

$$C_{\text{g,full cell}}(\text{F g}^{-1}) = \frac{\int i \, dt}{m_{\text{total}} V_{\text{cell}}} \quad (3)$$

where *m_{total}* is the mass of active material on both electrodes and *V_{cell}* is the voltage window of the full cell. The volumetric capacitance of the full cell is calculated on the basis of *C_{v,full cell}* = *C_{g,full cell}* × (mass of the active materials on both electrodes/volume of the active materials on both electrodes).

The energy density of the full cell was estimated on the basis of the anodic scan of the CV (*E_{CV}*) and discharge branch of the GCD curve (*E_{GCD}*), and

$$E_{\text{CV}} = \left(\int_{V_0}^{V_{\text{max}}} i \, dV \right) \Delta \tau \quad (4)$$

$$E_{\text{GCD}} = I_c \left(\int_{V_0}^{V_{\text{max}}} t \, dV \right) \quad (5)$$

where Δ*τ* in equation (4) is the charge–discharge time determined by the sweep rate³⁵, and the *I_c* in equation (5) is the constant discharge current density. *V₀* to *V_{max}* is the voltage window of the full cell. The average power density was further evaluated on the basis of *P* = *E*/Δ*t*.

MD simulations. MD simulations in a charged state in the presence of the different electrolytes were performed using the in situ XRD measured interlayer separation in the charged state and the charge stored per gram of macroporous Ti₃C₂. The charge contributed by the formation of the electrical double layer is excluded from the MD simulation, as cation–anion exchange and anion desorption may also contribute to the double-layer capacitance^{36,37}.

To investigate the microscopic origins of the solvent dependence of MXene capacitance in LiTFSI solutions, we used classical non-reactive MD simulations in the NPT ensemble (that is, at constant temperature and pressure). The reference surface composition was set to that of the previously analysed HF10 system³⁸, with a mixture of O, OH and F terminal groups, where the relative fraction of O/OH groups was varied to compensate for the Li⁺ charges by deprotonation. The number of intercalated Li ions (excluding electrical double-layer capacitance) was fixed at the experimentally determined values of 0.37, 0.46 and 0.93 cations per MXene unit (Ti₃C₂(O,OH,F)₂) for ACN, DMSO and PC solvents on macroporous Ti₃C₂, respectively. The amount of solvent within the pores was adjusted to reproduce the experimentally found interlayer separation determined by XRD. The exact amount of solvent was adjusted by performing multiple simulations equilibrated at *P* = 1 bar and *T* = 298.15 K with different numbers of solvent molecules and choosing the one whose resulting equilibrium lattice constant agreed most closely with the experimental value.

The interactions between MXene atoms were described by an in-house force field optimized to reproduce pair distribution functions generated in density functional theory (DFT)-MD simulations, and tested against experimentally measured structural properties of pristine MXenes³⁸. The force-field functional form consisted of the Lennard-Jones potential, point charges, harmonic bonds and harmonic angles, with parameters listed in Supplementary Tables 1–3. For the interactions of pure DMSO and ACN solvents and their interactions with Li ions, we used a force field previously adjusted to study lithium solvation in a DMSO–ACN mixture, with parameters given in the original literature³⁹. The cross-interaction parameters of size (*σ_{ij}*) and energy (*ε_{ij}*) between MXene and the electrolyte solution (Li ions and solvents) were determined using the Lorentz–Berthelot combining rules:

$$\sigma_{ij} = \frac{\sigma_i + \sigma_j}{2}; \quad \epsilon_{ij} = \sqrt{\epsilon_i \epsilon_j} \quad (6)$$

where *σ_{ij}* and *ε_{ij}* are the size and energy parameters of the Lennard-Jones potential for atom *i* (or *j*), respectively. Long-ranged Coulombic interactions were calculated using the Ewald method. The simulations were performed under a constant pressure of 100 kPa and temperature of 298.15 K, with the integration time step of 1 fs. The simulation box contained 5,314 MXene atoms forming two

independent plates, while the numbers of Li ions and solvent molecules varied according to the system. For the PC-based system, we tried to introduce a trace amount of PC molecules into the interlayer space in the simulation. We observed a sudden expansion of the *d*-spacing calculated by MD simulation, similar to the ACN system. This further confirm that the Li ions confined between MXene layers must be fully desolvated when using the PC-based electrolyte.

Data availability

The data that support the plots within this paper and other findings of this study are available from the corresponding author upon reasonable request.

Received: 12 September 2018; Accepted: 25 January 2019;

Published online: 04 March 2019

References

- Simon, P. & Gogotsi, Y. Materials for electrochemical capacitors. *Nat. Mater.* **7**, 845–854 (2008).
- Simon, P., Gogotsi, Y. & Dunn, B. Where do batteries end and supercapacitors begin? *Science* **343**, 1210–1211 (2014).
- Salanne, M. et al. Efficient storage mechanisms for building better supercapacitors. *Nat. Energy* **1**, 16070 (2016).
- Lukatskaya, M. R., Dunn, B. & Gogotsi, Y. Multidimensional materials and device architectures for future hybrid energy storage. *Nat. Commun.* **7**, 12647 (2016).
- Nitta, N., Wu, F., Lee, J. T. & Yushin, G. Li-ion battery materials: present and future. *Mater. Today* **18**, 252–264 (2015).
- Zhu, Y. et al. Carbon-based supercapacitors produced by activation of graphene. *Science* **332**, 1537–1541 (2011).
- Zhong, C. et al. A review of electrolyte materials and compositions for electrochemical supercapacitors. *Chem. Soc. Rev.* **44**, 7484–7539 (2015).
- Mourad, E. et al. Biredox ionic liquids with solid-like redox density in the liquid state for high-energy supercapacitors. *Nat. Mater.* **16**, 446–453 (2017).
- Choi, D., Blomgren, G. E. & Kumta, P. N. Fast and reversible surface redox reaction in nanocrystalline vanadium nitride supercapacitors. *Adv. Mater.* **18**, 1178–1182 (2006).
- Wang, G., Zhang, L. & Zhang, J. A review of electrode materials for electrochemical supercapacitors. *Chem. Soc. Rev.* **41**, 797–828 (2012).
- Augustyn, V., Simon, P. & Dunn, B. Pseudocapacitive oxide materials for high-rate electrochemical energy storage. *Energy Environ. Sci.* **7**, 1597–1614 (2014).
- Anasori, B., Lukatskaya, M. R. & Gogotsi, Y. 2D metal carbides and nitrides (MXenes) for energy storage. *Nat. Rev. Mater.* **2**, 16098 (2017).
- Lukatskaya, M. R. et al. Ultra-high-rate pseudocapacitive energy storage in two-dimensional transition metal carbides. *Nat. Energy* **2**, 17105 (2017).
- Lin, Z. et al. Capacitance of Ti₃C₂T_x MXene in ionic liquid electrolyte. *J. Power Sources* **326**, 575–579 (2016).
- Dall'Agness, Y., Rozier, P., Taberna, P.-L., Gogotsi, Y. & Simon, P. Capacitance of two-dimensional titanium carbide (MXene) and MXene/carbon nanotube composites in organic electrolytes. *J. Power Sources* **306**, 510–515 (2016).
- Kajiyama, S. et al. Enhanced Li-ion accessibility in MXene titanium carbide by steric chloride termination. *Adv. Energy Mater.* **7**, 1601873 (2017).
- Wang, X. et al. Geometrically confined favourable ion packing for high gravimetric capacitance in carbon–ionic liquid supercapacitors. *Energy Environ. Sci.* **9**, 232–239 (2016).
- Chmiola, J. et al. Anomalous increase in carbon capacitance at pore sizes less than 1 nanometer. *Science* **313**, 1760–1763 (2006).
- Brouillette, D., Perron, G. & Desnoyers, J. E. Effect of viscosity and volume on the specific conductivity of lithium salts in solvent mixtures. *Electrochim. Acta* **44**, 4721–4742 (1999).
- Gogotsi, Y. & Penner, R. M. Energy storage in nanomaterials—capacitive, pseudocapacitive, or battery-like? *ACS Nano* **12**, 2081–2083 (2018).
- Segalini, J., Daffos, B., Taberna, P.-L., Gogotsi, Y. & Simon, P. Qualitative electrochemical impedance spectroscopy study of ion transport into sub-nanometer carbon pores in electrochemical double layer capacitor electrodes. *Electrochim. Acta* **55**, 7489–7494 (2010).
- Taberna, P., Simon, P. & Fauvarque, J.-F. Electrochemical characteristics and impedance spectroscopy studies of carbon–carbon supercapacitors. *J. Electrochem. Soc.* **150**, A292–A300 (2003).
- Okubo, M., Sugahara, A., Kajiyama, S. & Yamada, A. MXene as a charge storage host. *Acc. Chem. Res.* **51**, 591–599 (2018).
- Cabana, J., Monconduit, L., Larcher, D. & Palacin, M. R. Beyond intercalation-based Li-ion batteries: the state of the art and challenges of electrode materials reacting through conversion reactions. *Adv. Mater.* **22**, E170–E192 (2010).
- Futamura, R. et al. Partial breaking of the Coulombic ordering of ionic liquids confined in carbon nanopores. *Nat. Mater.* **16**, 1225 (2017).
- Come, J. et al. Controlling the actuation properties of MXene paper electrodes upon cation intercalation. *Nano Energy* **17**, 27–35 (2015).
- Jäckel, N. et al. Electrochemical in situ tracking of volumetric changes in two-dimensional metal carbides (MXenes) in ionic liquids. *ACS Appl. Mater. Interfaces* **8**, 32089–32093 (2016).
- Levi, M. D. et al. Solving the capacitive paradox of 2D MXene using electrochemical quartz-crystal admittance and in situ electronic conductance measurements. *Adv. Energy Mater.* **5**, 1400815 (2015).
- Brousse, T., Bélanger, D. & Long, J. W. To be or not to be pseudocapacitive? *J. Electrochem. Soc.* **162**, A5185–A5189 (2015).
- Ghidiu, M., Lukatskaya, M. R., Zhao, M.-Q., Gogotsi, Y. & Barsoum, M. W. Conductive two-dimensional titanium carbide ‘clay’ with high volumetric capacitance. *Nature* **516**, 78–81 (2014).
- Park, S. H., Kim, J., Lee, W.-E., Byun, D.-J. & Kim, M. H. One-step synthesis of hollow dimpled polystyrene microparticles by dispersion polymerization. *Langmuir* **33**, 2275–2282 (2017).
- Alhabej, M. et al. Guidelines for synthesis and processing of two-dimensional titanium carbide (Ti₃C₂T_x MXene). *Chem. Mater.* **29**, 7633–7644 (2017).
- Li, K., Liu, J., Huang, Y., Bu, F. & Xu, Y. Integration of ultrathin graphene/polyaniline composite nanosheets with a robust 3D graphene framework for highly flexible all-solid-state supercapacitors with superior energy density and exceptional cycling stability. *J. Mater. Chem. A* **5**, 5466–5474 (2017).
- Meyer, A., Dimeo, R., Gehring, P. & Neumann, D. The high-flux backscattering spectrometer at the NIST Center for Neutron Research. *Rev. Sci. Instrum.* **74**, 2759–2777 (2003).
- Mitchell, J. B., Lo, W. C., Genc, A., LeBeau, J. & Augustyn, V. Transition from battery to pseudocapacitor behavior via structural water in tungsten oxide. *Chem. Mater.* **29**, 3928–3937 (2017).
- Forse, A. C., Merlet, C., Griffin, J. M. & Grey, C. P. New perspectives on the charging mechanisms of supercapacitors. *J. Am. Chem. Soc.* **138**, 5731–5744 (2016).
- Forse, A. C. et al. Direct observation of ion dynamics in supercapacitor electrodes using in situ diffusion NMR spectroscopy. *Nat. Energy* **2**, 16216 (2017).
- Wang, H.-W., Naguib, M., Page, K., Wesolowski, D. J. & Gogotsi, Y. Resolving the structure of Ti₃C₂T_x MXenes through multilevel structural modeling of the atomic pair distribution function. *Chem. Mater.* **28**, 349–359 (2015).
- Semino, R., Zaldivar, G., Calvo, E. J. & Laria, D. Lithium solvation in dimethyl sulfoxide–acetonitrile mixtures. *J. Chem. Phys.* **141**, 214509 (2014).

Acknowledgements

The research was sponsored by the Fluid Interface Reactions, Structures, and Transport (FIRST) Center, an Energy Frontier Research Center (EFRC) funded by the US Department of Energy, Office of Science, and Office of Basic Energy Sciences. Access to the HFBS was provided by the Center for High Resolution Neutron Scattering, a partnership between the NIST and the NSF under agreement no. DMR-1508249. Certain commercial equipment, instruments or materials are identified in this paper in order to specify the experimental procedure adequately. Such identification is not intended to imply recommendation or endorsement by the National Institute of Standards and Technology, nor is it intended to imply that the materials or equipment identified are necessarily the best available for the purpose. J. Li and H. Wang from Drexel University are acknowledged for helping with material characterization. Y. Honda and Y. Soda from Murata Manufacturing Co. are acknowledged for helpful discussions and help with the characterization.

Author contributions

X.W. and Y.G. planned the study. X.W., T.S.M., Z.L. and T.T. conducted electrochemical testing. K.L. synthesized all MXenes. Z.L. performed the in situ XRD measurement and L.V. performed the MD simulation. C.H., P.U. and A.S. performed TEM, XPS and Raman investigations, respectively. N.C.O., M.T. and E.M. performed the neutron scattering. All authors contributed to writing the manuscript under supervision from P.S. and Y.G.

Competing interests

The authors declare no competing interests.

Additional information

Supplementary information is available for this paper at <https://doi.org/10.1038/s41560-019-0339-9>.

Reprints and permissions information is available at www.nature.com/reprints.

Correspondence and requests for materials should be addressed to Y.G.

Publisher's note: Springer Nature remains neutral with regard to jurisdictional claims in published maps and institutional affiliations.

© The Author(s), under exclusive licence to Springer Nature Limited 2019